Error analysis of stress-strain characterisation on solid-state polymers under simple shear deformation using V-Notched Rail shear test

Hongyan Wang [a], Zerong Ding [a], Haibao Liu [b], Nan Li [a,*]

[a] Dyson School of Design Engineering, Imperial College London, Exhibition Road, London. SW7 2DB, UK

[b] Centre for Aeronautics, School of Aerospace, Transport and Manufacturing, Cranfield University, Cranfield, MK43 0AL, UK

Abstract

In the present research, the errors for characterising the stress-strain behaviour under simple shear deformation are identified via theoretical analysis and experimental and numerical studies, based on the V-Notched Rail (VNR) shear tests performed on the solid-state Poly-Ether-Ether-Ketone (PEEK). By analysing the stress-strain behaviour of PEEK obtained from numerical simulations, the errors caused by the rotation factor and the nonuniformity factor are mathematically linked to the deformation. A two-step correction method is proposed to correct the calculation errors and, therefore, to obtain real stress-strain behaviour. This correction method is then validated using the VNR shear test conducted on the PEEK. Besides, this correction method is also examined by two sets of VNR shear simulations performed at a different testing condition with PEEK and on a different material (Polyamide 6, PA6). Both numerical and experimental results show that, at large deformation (when the effective strain is higher than 0.1) of solid-state polymers under VNR shear deformation, the calculation errors are nonnegligible, and the proposed two-step correction method can correct the VNR shear test results. To the best of the authors' knowledge, this research is the first time to thoroughly analyse the simple shear deformation, and evaluate the calculation errors on the effective stress-strain properties of solid-state polymers characterised through the VNR shear tests. The proposed two-step correction method is proven to be robust and can be adapted to other solid-state polymers under different testing conditions.

Keywords

Simple shear; V-Notched Rail (VNR) shear test; large deformation; stress-strain behaviour; two-step correction.

1. Introduction

Material characterisation methods on sheet materials are worthy of study for various engineering applications, of which the stress-strain responses under shear loading have been attracting great interests [1]. In shear deformation interpretation, pure shear and simple shear are two distinct concepts and need to be discriminated when evaluating the mechanical behaviour from shear tests [2]. The commonly used shear test methods on sheet materials, such as the V-Notched Rail (VNR) shear test according to ASTM 7078 [3], the two rail and three rail tests according to ASTM D4255 [4, 5], and the Iosipescu test according to ASTM D5379 [6, 7], are all based on simple shear deformation. For these shear test methods, many researchers considered simple shear as a combination of pure shear and rigid-body rotation within small deformation [8, 9]. However, this simplification is not applicable to large deformations [1] and will cause calculation errors. The calculation errors and corresponding correction methods are required to study for further understanding, especially for polymers, as there is an increasing application of polymers and Polymer Matrix Composites (PMCs) for lightweight panel components, and for both materials the forming process involves large deformation [10]. In addition, as mentioned by several researchers [2,

11, 12], deviatoric stresses have more influence on the mechanical behaviour of polymers, which confirms the significance of accurately characterising the stress-strain response of polymers under shear loading.

For the fundamental understanding of the simple shear deformation, Thiel et al. [2] explained the incompatibility of Cauchy pure shear stress and simple shear deformation. Also, they introduced the notion of idealised finite simple shear form that can be applied to certain classes of hyperelastic materials under plane stress conditions without pressure, such as the Mooney-Rivlin material. Belytscho et al. [13] presented solutions to simple shear problems by introducing the objective stress rates on hyperelastic materials; however, the equations for solving the stress state under simple shear deformation were complicated, and different results would be obtained by using various objective stress rates. To study the deformation of a cylinder without axial load, Rajagopal et al. [14] established the shear strain field of the simple shear deformation in the form of stretch ratios along the principal axes of the nonlinear isotropic elastic material. The comparison between the simple shear and the pure shear on a hyperelastic material under large deformation was conducted by Moreira et al. [1]. In their research, the simple shear deformation was achieved by a single lap joint test, and the pure shear deformation was obtained using the planar tension test. Although the above studies have provided insights into the deformation mechanisms of simple shear and identified the differences between simple shear and pure shear, the stress and strain state of materials under simple shear are still unclear, not to mention a unified post-processing method.

For the stress-strain behaviour calculated from simple shear tests, there are studies that indicated several error sources. The rotation of principal strains under simple shear deformation was reported by G'Sell et al. [15] and Dayan et al. [9]. Due to the existence of principal strains' rotation, the directions of the principal stresses also rotate continuously during the simple shear test. As a result, the effective stress that calculated according to pure shear deformation is not accurate anymore. In addition to the error due to rotation, Hedner et al. [16] reported that the shear stresses were not uniformly distributed when simulating the simple shear deformation of polymers. This nonuniform deformation could affect the effective stress-strain calculation results if the stress localisation was not well addressed. Melin et al. [17] also mentioned the calculation errors generated by the nonuniform deformation. To achieve a more uniform deformation, they redesigned the Iosipescu test specimen by rescaling the opening angle of the test specimen according to the orthotropic ratio, which is the ratio of the two in-plane principal Young's moduli. For the post-processing of testing data and the correction of these calculation errors, several methods have been proposed by giving correction factors to improve the accuracy of calculations. For example, Oh et al. [18] identified the strain measurement errors while conducting the Iosipescu test on Carbon/Epoxy composites, which resulted in an error with measured shear modulus. They defined a correction factor which was denoted as the ratio of the average strain over the central area to the central point strain of the testing specimen, based on the Finite Element Analysis (FEA) results, to obtain a more precise shear modulus. Taheri-Behrooz et al. [19] also used similar correction factors to correct the nonuniformity-

induced shear stresses via FEA. However, these correction factors are usually fixed numbers and can only be applied to specific testing materials and conditions. In summary, although there are studies that have pointed out several error sources of simple shear tests and proposed correct solutions, none of them proposed a universal correction method that suited for a variety of materials under a simple shear test method.

The objectives of this research are to show the errors during the VNR shear tests on polymers, give a detailed analysis of the error sources, and then present a universal post-processing method to calculate the effective stress-strain properties of solid-state polymers using the VNR shear tests. The structure of this paper is as follows. Section 2 presents experimental investigations on solid-state polymers to offer a ground truth of the properties of the studied material and present the errors at large deformation if use the traditional calculation method. Section 3 gives a detailed theoretical analysis of the error source and approaches of strain measurement. After understanding the research problem, the numerical simulation of the VNR shear deformation is presented in Section 4, so that a full field of the stress-strain data can be obtained and the corresponding mechanism articulated in section 3 can be better understood. And using the full field stress-strain date shown in section 4, a two-step correction method is proposed and validated in Section 5. Section 6 lists the key conclusions of this study.

2. Experimental investigation

Two sets of experiments were designed and conducted for the following purposes:

1) Tensile test. The tensile tests were conducted, as the tensile test is a common material characterisation practice to study the material behaviour [11]. From the tensile test results, a benchmark of the solid-state polymers can be established, so that the calculation errors of the VNR shear tests from the traditional calculation method can be visualised, and the numerical simulation can be conducted by using the constitutive model from the benchmark results.
2) The VNR shear test. By conducting the VNR test and comparing the stress-strain properties calculated from the VNR shear test via traditional method, the calculation errors can be visualised clearly. Besides, the VNR shear test results will be used for validating the numerical simulation, and validating the correction method proposed in this research.

2.1. Materials and specimens

The PEEK and PA6 polymers were selected as the experimental materials. Both polymers are semicrystalline thermoplastics that are widely used as structural component materials or the matrices in thermoplastic polymer matrix composites (TPMCs). With these wide applications, there is a high demand for characterising the mechanical behaviour of these thermoplastics under shear loading. In this study, the PEEK and PA6 materials were supplied as 2 mm and 5.5 mm thick sheets, by Ai Engineering Plastics & Laminates and Direct Plastics in the UK, respectively.

Tensile testing specimens were designed according to the standard testing method defined by ASTM 638 [20]. The tensile testing specimen and its dimensions are shown in Fig. 1a and 1b, respectively. Two holes were machined on the specimen at the two ends for mounting onto the bespoke lightweight grips. For the VNR shear test, as reported by Nunes et al. [12] and Daiyan et al. [9], there was severe distortion during deformation in the standard test specimen defined in ASTM 7078 [3]. This was also observed by conducting the VNR shear test on PEEK using the standard specimen in this study. Thus, to avoid specimen distortion and to achieve a larger deformation, a modification was made on the specimen design by reducing the ligament length. The dimensions of the modified VNR shear specimen are shown in Fig. 1c. Two deep notches were machined on the standard specimens. The ligament length of the modified specimen is 15.68 mm. The modified shear test specimen with the shear test grips is shown in Fig. 1d. While mounting the specimen to the fixtures during the VNR shear experiment, a pair of space blocks were used to guarantee the good alignment between the specimen ligament and the loading axis. Besides, special care was taken while tightening the bolts in the VNR shear grips to avoid any out-of-plane twisting.

2.2. Testing procedure of tensile and VNR shear experiments

Both tensile and shear tests were performed on an INSTRON 5584 universal tensile testing machine shown in Fig. 1e. An environmental chamber was mounted on the machine to heat the test specimen to the target temperatures. The temperature of the specimen was monitored by thermocouples connected to a data-logger during the experiments. A camera was used to record the testing images for strain measurements, at a recording speed of 60 frame-per-second (fps). A light source was also used to assist the image recording. Fans were used to prevent the overheating of the load cell and the machine itself. To achieve a large deformation in the shear experiments, the tests were conducted at evaluated temperatures between the glass transition temperature (T_g, 143 ℃ for PEEK, 47 ℃ for PA6) and melting temperature (T_m, 343 ℃ for PEEK, 230 ℃ for PA6). First, for the characterisation purpose, the tensile and the VNR shear tests were conducted on PEEK at 180 ℃, at a starting strain rate of 0.1 /s, with the crosshead speed set as 2.54 mm/s for the tensile tests, and 1.57 mm/s for the VNR shear tests. Second, for the validation purpose, tensile tests were conducted on PEEK at 240 ℃ and on PA6 at 160 ℃, both at a strain rate of 0.1 /s. The consistency of experimental results was examined by repeating tests on these materials under their corresponding testing conditions.

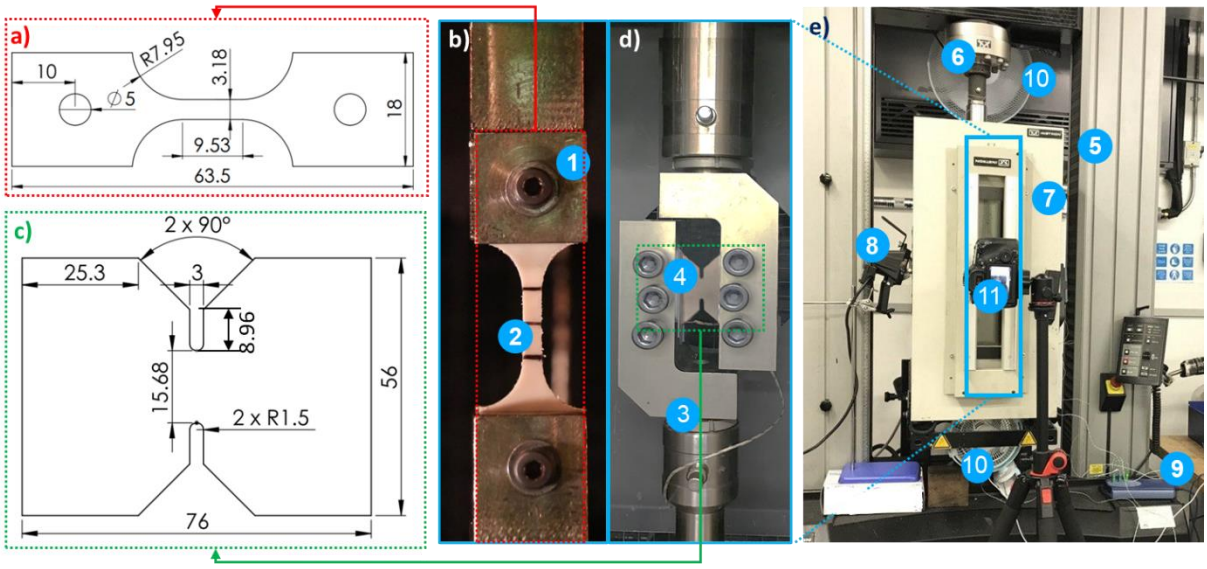

Fig. 1. The experimental setup and specimen designs for the tensile and the VNR shear tests. The a) design and dimensions (unit: mm) and b) an example picture of the specimen and grip for the tensile test; the c) design and dimensions (unit: mm) and d) an example picture of the specimen and grip for the VNR shear test; e) Experimental setup: ①Tensile test grip; ②Tensile test specimen; ③VNR shear test grip; ④VNR shear test specimen; ⑤Instron 5584 load frame; ⑥Crosshead embedded with a load cell; ⑦Environmental chamber; ⑧Light; ⑨Thermocouples and data-logger; ⑩Fan; ⑪Camera.

For both tensile and shear tests, the digital image correlation (DIC) method was used for the strain measurement. In the tensile tests, three lines were drawn on the test specimen shown in Fig. 2a. The 1st and the 3rd lines marked the two ends of the gauge length (7.62 mm at the undeformed state), and the 2nd line was drawn in the middle to assist the image processing. The image processing method was implemented using a self-developed MATLAB script according to the method introduced in Wang et al. [21]. The positions of the three lines were tracked during the tests, based on which the tensile strain within the gauge length can be calculated.

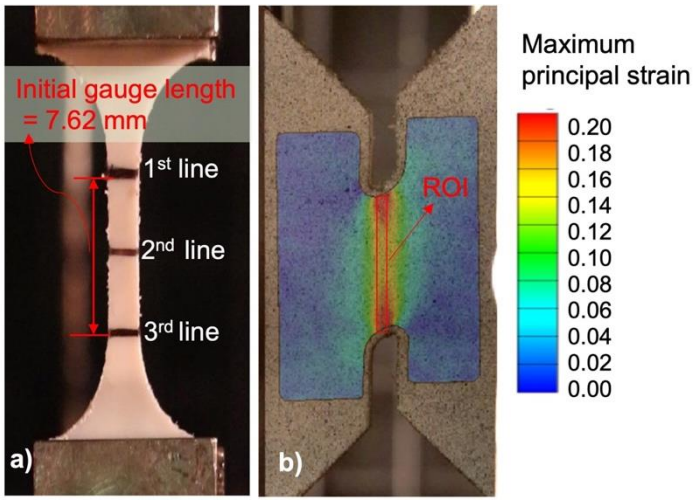

Fig. 2. The *in-situ* measurement methods for a) the tensile test and b) the VNR shear test.

In the VNR shear test, the test images were captured at a resolution of around 225 pixels/mm^2 and processed by a two-dimensional (2D) DIC software, provided by GOM, Germany. A facet size of 16 × 16 pixels with a distance of 14 pixels was defined in the software to create a surface component for

further calculation. For each facet, the software automatically calculated its strain state on the central point of the facet at each deformation stage. Therefore, the strain field can be extracted, as shown in Fig. 2b. The ROI was defined as the central section of the specimen at a length of the maximum recognisable length and a width of around 1 mm. The effective strain of the ROI at each deformation stage was defined by the arithmetic mean of the maximum principal strains within the ROI. According to the observation of experiments, it was confirmed that the DIC processing method was robust enough and slight change of camera position for each set of experiment would not impact the processing results.

2.3. Experimental results

To have an impression on that the calculation error would be introduced by following the standard post-processing method of the VNR shear test, the effective stress-strain properties were evaluated. For both tensile and shear test results, the effective strain and effective stress were defined as the von-Mises effective strain ($\bar{\varepsilon}$) according to Eq.(1) and effective stress ($\bar{\sigma}$) according to Eq. (2) respectively. The detailed calculation process is listed in Table 1.

$$\bar{\varepsilon} = \frac{\sqrt{2}}{3}\sqrt{(\varepsilon_1 - \varepsilon_2)^2 + (\varepsilon_2 - \varepsilon_3)^2 + (\varepsilon_3 - \varepsilon_1)^2} \quad (1)$$

$$\bar{\sigma} = \frac{\sqrt{2}}{2}\left(\sqrt{(\sigma_1 - \sigma_2)^2 + (\sigma_2 - \sigma_3)^2 + (\sigma_3 - \sigma_1)^2}\right) \quad (2)$$

Table 1. The detailed effective stress-strain calculation for the tensile and the VNR shear tests

Variables	The tensile test		The VNR shear test	
Measured variables	• Vertical load (F^t) • Initial cross-section area (A_0^t) • Engineering tensile strain ε_{eng}^t calculated from gauge length (l) change		• Vertical Load (F^s) • Initial cross-section area (A_0^s) • Mean value of maximum principal strains (engineering strain) within the ROI ($\bar{\varepsilon}_{ROI}$) captured by GOM software	
Ture strain	$\varepsilon_{true}^t = \ln(1 + \varepsilon_{eng}^t)$	(3)	$\varepsilon_{true}^s = \ln(1 + \bar{\varepsilon}_{ROI})$	(4)
Principal strains	$\varepsilon_1^t = \varepsilon_{true}^t$ $\varepsilon_2^t = -\varepsilon_1^t/2$ $\varepsilon_3^t = -\varepsilon_1^t/2$	(5)	$\varepsilon_1^s = \varepsilon_{true}^s$ $\varepsilon_2^t = 0$ $\varepsilon_2^t = -\varepsilon_1^s$	(6)
Effective strain	$\bar{\varepsilon}_{\text{true}}^t = \varepsilon_1^t$	(7)	$\bar{\varepsilon}_{\text{true}}^t = \frac{2}{\sqrt{3}}\varepsilon_1^s$	(8)
True stress	$\sigma_{true}^t = \frac{F}{A_0^t} * (1 + \varepsilon_{eng}^t)$	(9)	$\sigma_{true}^s = \frac{F}{A_0^s} * (1 + \varepsilon_{ROI}^s)$	(10)
Principal stresses	$\sigma_1^t = \sigma_{true}^t$ $\sigma_2^t = 0$ $\sigma_3^t = 0$	(11)	$\sigma_1^s = \sigma_{true}^s$ $\sigma_2^s = 0$ $\sigma_3^s = -\sigma_{true}^s$	(12)
Effective stress	$\bar{\sigma}_{\text{true}}^t = \sigma_1^t$	(13)	$\bar{\sigma}_{\text{true}}^s = \sqrt{3}\sigma_1^s$	(14)

The effective stress-strain curves obtained from the tensile and the VNR shear tests on the PEEK specimens at 180 ℃ and 0.1 /s are shown in Fig. 3. As can be observed, there are obvious differences

between the effective stress-strain curves obtained from the tensile and VNR shear characterisation. Various error sources can cause these differences. As the potential error sources, such as the machining and measurement deviation, have been minimised with considerable efforts in this study, the calculation errors in the VNR shear test are deemed to exist for these obvious differences. To gain insight into the stress and strain state, the detailed theoretical analysis is presented in Section 3.

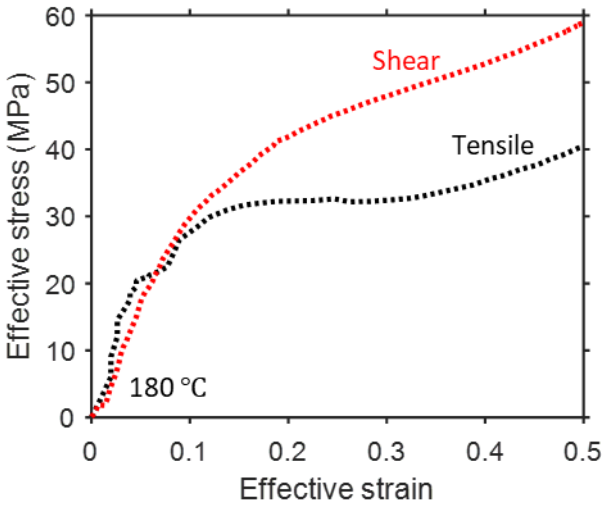

Fig. 3. The effective stress-strain curves obtained from the tensile and the VNR shear tests on PEEK at a temperature of 180 ℃ and at a strain rate of 0.1 /s.

3. A detailed explanation of VNR shear tests for stress-strain characterisation problem

This section will give a detailed explanation of the error sources that introduced from theoretical analysis. Besides, because of practical experimental procedure, the stress and strain measurement can also affect the calculation results. Therefore, the strain measurement methods are also explained to severe for the later work on proposing a universal correction method that can be adopted under different experimental approaches.

3.1. Deformation mechanism of the VNR shear specimen

The deformation mechanism of the VNR shear specimen can be understood from two aspects: the stress and deformation state within an infinitesimal element; and the overall strain distribution within the whole deformed area on the specimen.

Fig. 4 illustrates the stress and deformation state within an infinitesimal element and the common practice for understanding the VNR shear deformation. The stress state and deformation state of the central infinitesimal element in the ligament of the specimen are presented in Fig. 4a. There is a vertical load F along the loading direction and a constraining force on the other side, making the central elements deform as simple shear deformation. To maintain the simple shear deformation, shear stress (σ_{12}) and normal stresses (σ_{11} and σ_{22}) exist within the analysed element. During experiment, the vertical load F is the measurable variable, which accounts for the vertical stress components σ_{12} and σ_{22}. The term γ_{m-s} is the maximum shear strain of an analysed element in simple shear deformation. For small deformation, to simplify the calculation, the simple shear is

normally simplified to pure shear with a rigid-body rotation, shown in Fig. 4b. The term γ_{m-p} denotes the maximum shear strain of an analysed element in pure shear. In pure shear deformation, there is only a shear stress σ_{12} in the analysed unit element. Therefore, the measured load F accounts for only the shear stress. Clearly, the effective stress-strain is easier to calculate from the pure shear deformation as the stress state is less complicated.

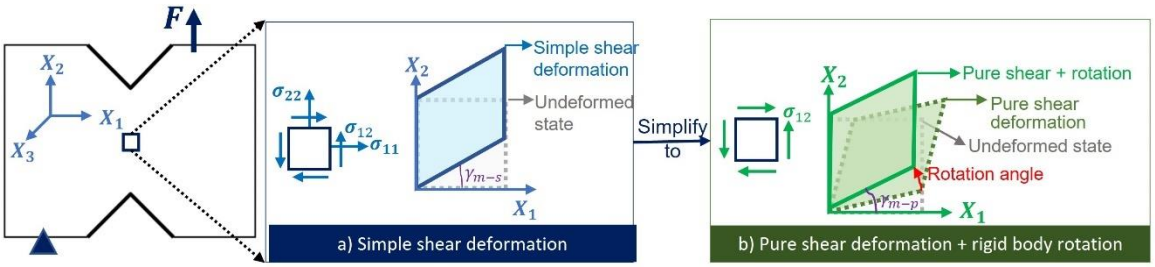

Fig. 4. Deformation mechanism of the VNR shear specimen. a) Simple shear deformation; b) Simplification of the deformation mechanism at small deformation: pure shear deformation + rigid body rotation. (Terms $\sigma_{11}, \sigma_{22}, \sigma_{12}$ are the stress components of the analysed element. Terms γ_{m-s} and γ_{m-p} are the maximum shear strains in simple shear and pure shear deformation, respectively.)

To understand the difference between simple shear and pure shear, the detailed analysis is shown in Fig. 5. The pure shear is shown in Fig. 5a. As for the simple shear deformation, since it combines stretch and rotation, RU polar decomposition will be analysed to isolate and understand the deformation mechanism, as illustrated in Fig. 5b.

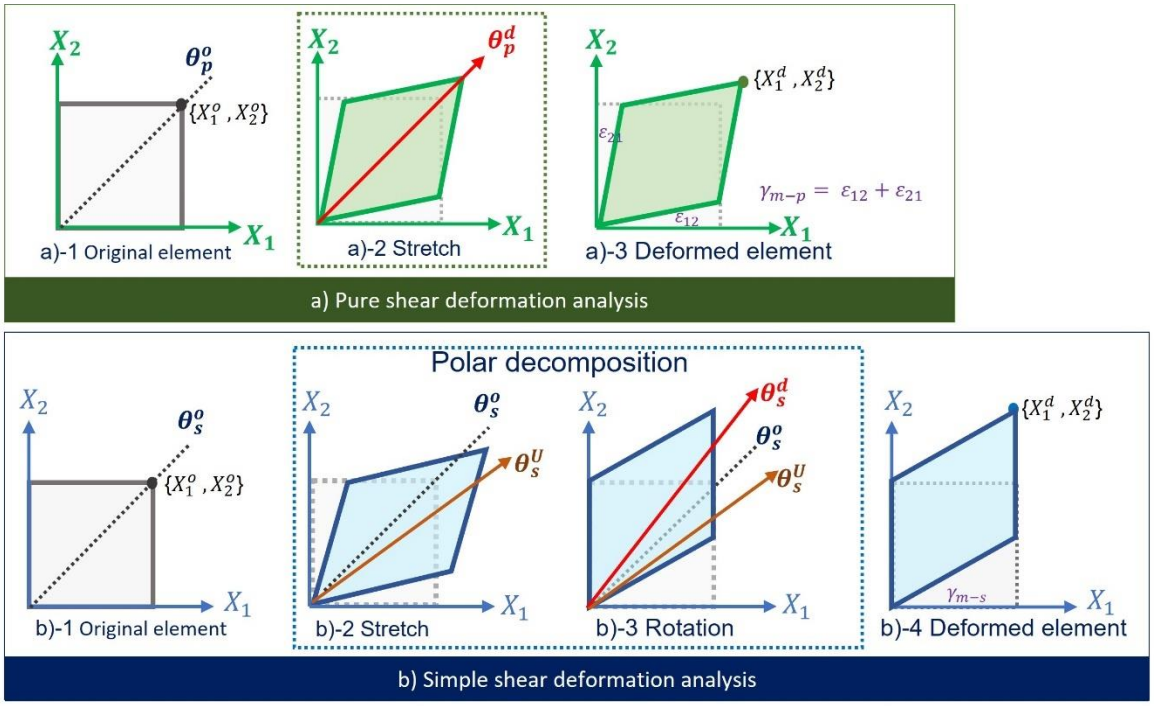

Fig. 5. Deformation mechanisms of a) Pure shear and b) Simple shear deformation. (The terms X_i^o, X_i^U, X_i^d $(i = 1,2,3)$ are the coordinates of the original, stretched, and deformed configurations, respectively. The arrows, $\boldsymbol{\theta_p^o}, \boldsymbol{\theta_p^d}$ represent the maximum principal strain directions of pure shear under original and deformed configurations, respectively; $\boldsymbol{\theta_s^o}$, $\boldsymbol{\theta_s^U}$, $\boldsymbol{\theta_s^d}$ are the maximum principal strain directions of simple shear under the original, stretched, and deformed configurations, respectively. Note: $\boldsymbol{\theta_p^o}$, $\boldsymbol{\theta_s^o}$ are two virtual directions for the

purpose of angle calculations. The terms $\gamma_{m-p}, \gamma_{m-s}$ are the maximum shear strain of the pure shear and simple shear deformation, respectively.)

By taking the central element as the analysed element, and using terms X_i^o, X_i^U, X_i^d $(i = 1,2,3)$ to represent the coordinates of the original, stretched, and deformed configurations, the coordinates of each configuration can be calculated according to the geometry change accordingly.

For pure shear deformation, by comparing Fig. 5a)-1 and a)-3 the in-plane coordinates of the deformed elements, X_1^d, X_2^d can be represented by Eq. (15-1):

$$X_1^d = X_1^o + X_2^o \cdot \tan\left(\frac{\gamma_{\max-\mathrm{p}}}{2}\right); \quad X_2^d = X_1^o \cdot \tan\left(\frac{\gamma_{\max-\mathrm{p}}}{2}\right) + X_2^o. \tag{15-1}$$

Based on the incompressible assumption[22] on solid-state polymers, X_3^d can be calculated as below:

$$X_3^d = \frac{|X_1^o||X_2^o|}{|X_1^d||X_2^d|} \cdot X_3^o. \tag{15-2}$$

Therefore, the relationship between the original configuration $\boldsymbol{X^o}$ and the deformed configuration $\boldsymbol{X^d}$, can be represented as Eq.*(16)*.

$$\boldsymbol{X^d} = \begin{bmatrix} 1 & \tan\left(\frac{\gamma_{m-p}}{2}\right) & 0 \\ \tan\left(\frac{\gamma_{m-p}}{2}\right) & 1 & 0 \\ 0 & 0 & \frac{1}{1-\tan^2\left(\frac{\gamma_{m-p}}{2}\right)} \end{bmatrix} \cdot \boldsymbol{X^o}. \tag{16}$$

And the deformation gradient of pure shear, F_p can be calculated accordingly:

$$\boldsymbol{F_p} = \frac{\partial \boldsymbol{X^d}}{\partial \boldsymbol{X^o}} = \begin{bmatrix} 1 & \tan\left(\frac{\gamma_{m-p}}{2}\right) & 0 \\ \tan\left(\frac{\gamma_{m-p}}{2}\right) & 1 & 0 \\ 0 & 0 & \frac{1}{1-\tan^2\left(\frac{\gamma_{m-p}}{2}\right)} \end{bmatrix}. \tag{17}$$

As shown in Eq. (17), the deformation gradient tensor of pure shear, $\boldsymbol{F_p}$, is symmetrical, which indicates that no rotation but only stretch exists in pure shear deformation. Therefore, the angle between the maximum principal strain and the X_1 axis remains 45° ($\boldsymbol{\theta_p^o}$, $\boldsymbol{\theta_p^d}$ in Fig. 5a)-2) all the time.

Similarly, for simple shear deformation, by comparing *Fig. 5*b)-1 and b)-4 the deformed configuration can be calculated as Eq. *(18)*.

$$X_1^d = X_1^o;\ X_2^d = \tan(\gamma_{m-s}) \cdot X_1^o + X_2^o;\ X_3^d = X_3^o \tag{18}$$

the deformation gradient tensor, $\boldsymbol{F_s}$, can be expressed as:

$$\boldsymbol{F_s} = \frac{\partial \boldsymbol{X^d}}{\partial \boldsymbol{X^o}} = \begin{bmatrix} 1 & 0 & 0 \\ \tan(\gamma_{m-s}) & 1 & 0 \\ 0 & 0 & 1 \end{bmatrix}. \tag{19}$$

Eq.(19) shows that the deformation gradient tensor of simple shear, $\boldsymbol{F_s}$, is asymmetric, which indicates that rotation exists during such deformation. After polar decomposition with $\boldsymbol{F_s}$, the rotation tensor $\boldsymbol{R}$ and stretch tensor $\boldsymbol{U}$, in a relation of $\boldsymbol{F_S = RU}$, can be obtained as below:

$$\boldsymbol{R}=\begin{bmatrix}\frac{1}{\sqrt{1+b^2}} & \frac{-b}{\sqrt{1+b^2}} & 0\\ \frac{b}{\sqrt{1+b^2}} & \frac{1}{\sqrt{1+b^2}} & 0\\ 0 & 0 & 1\end{bmatrix};\quad \boldsymbol{U}=\begin{bmatrix}\frac{1+2b^2}{\sqrt{1+b^2}} & \frac{b}{\sqrt{1+b^2}} & 0\\ \frac{b}{\sqrt{1+b^2}} & \frac{1}{\sqrt{1+b^2}} & 0\\ 0 & 0 & 1\end{bmatrix} \tag{20}$$

The stretch process is illustrated in Fig. 5b)-2, the eigenvectors of $\boldsymbol{U}$ are the directions principal strains, and of which the first eigenvector, $\widehat{\boldsymbol{v}}_{\boldsymbol{1}}$, is corresponding to $\boldsymbol{\theta}_{\boldsymbol{s}}^{\boldsymbol{l}}$ (l refers to 'o', 'U' for original and deformed configurations, respectively) illustrated in Fig. 5b. $\widehat{\boldsymbol{v}}_{\boldsymbol{1}}$ can be expressed as Eq. *(21)*.

$$\widehat{\boldsymbol{v}}_{\boldsymbol{1}}=\begin{bmatrix}\sqrt{1+b^2}+b\\ 1\\ 0\end{bmatrix}. \tag{21}$$

The direction of the maximum principal strain, $\widehat{\boldsymbol{v}}_{\boldsymbol{1}}$, can be understood as below:

- In the original configuration, as shown in Fig. 5b)-1, $b=0$, therefore, $\widehat{\boldsymbol{v}}_{\boldsymbol{1}}=[1\ 1\ 0]^T$, which means $\widehat{\boldsymbol{v}}_{\boldsymbol{1}}$ is at a direction of 45° with the X_1 axis, shown as $\boldsymbol{\theta}_{\boldsymbol{s}}^{\boldsymbol{o}}$. It is worth mentioning that $\boldsymbol{\theta}_{\boldsymbol{s}}^{\boldsymbol{o}}$ is listed in the figure only for the purpose of calculating the rotation angle of the principal strain and no actual physical meaning is represented.
- In the stretched configuration, as shown in *Fig. 5*b)-2, the angle between the maximum principal strain and the X_1 axis, i.e. the angle between $\boldsymbol{\theta}_{\boldsymbol{s}}^{\boldsymbol{U}}$ and X_1 axis, can be calculated according to $\widehat{\boldsymbol{v}}_{\boldsymbol{1}}$:

$$\tan(\boldsymbol{\theta}_{\boldsymbol{s}}^{\boldsymbol{U}})=\frac{1}{\sqrt{1+b^2}+b}=\sqrt{1+b^2}-b; \tag{22}$$

Accordingly, from *Fig. 5*b)-1 to b)-2, the change of the direction of maximum principal strain can be calculated:

$$\tan(\boldsymbol{\theta}_{\boldsymbol{s}}^{\boldsymbol{oU}})=\tan(\boldsymbol{\theta}_{\boldsymbol{s}}^{\boldsymbol{U}}-\boldsymbol{\theta}_{\boldsymbol{s}}^{\boldsymbol{o}})=\frac{\tan(\boldsymbol{\theta}_{\boldsymbol{s}}^{\boldsymbol{U}})-\tan(\boldsymbol{\theta}_{\boldsymbol{s}}^{\boldsymbol{o}})}{1+\tan(\boldsymbol{\theta}_{\boldsymbol{s}}^{\boldsymbol{U}})\cdot\tan(\boldsymbol{\theta}_{\boldsymbol{s}}^{\boldsymbol{o}})}=\frac{1-\sqrt{1+b^2}}{b} \tag{23}$$

The rotation process is illustrated in Fig. 5b)-3. The counterclockwise rotational angle of the analysed element (i.e., the rigid body rotation) $\boldsymbol{\theta}_{\boldsymbol{s}}^{\boldsymbol{Ud}}=\boldsymbol{\theta}_{\boldsymbol{s}}^{\boldsymbol{d}}-\boldsymbol{\theta}_{\boldsymbol{s}}^{\boldsymbol{U}}$. According to the definition of rational tensor $\boldsymbol{R}$, in the form of $\boldsymbol{\theta}_{\boldsymbol{s}}^{\boldsymbol{Ud}}$, $\boldsymbol{R}$ can be represented as:

$$R=\begin{bmatrix}\cos(\boldsymbol{\theta}_{\boldsymbol{s}}^{\boldsymbol{Ud}}) & -\sin(\boldsymbol{\theta}_{\boldsymbol{s}}^{\boldsymbol{Ud}}) & 0\\ \sin(\boldsymbol{\theta}_{\boldsymbol{s}}^{\boldsymbol{Ud}}) & \cos(\boldsymbol{\theta}_{\boldsymbol{s}}^{\boldsymbol{Ud}}) & 0\\ 0 & 0 & 1\end{bmatrix} \tag{24}$$

By comparing Eqs. *(20)* and *(24)*, $\boldsymbol{\theta}_{\boldsymbol{s}}^{\boldsymbol{Ud}}$ can be calculated as below:

$$\tan(\boldsymbol{\theta}_{\boldsymbol{s}}^{\boldsymbol{Ud}})=b. \tag{25}$$

It is found from Eq. *(25)* that

$$\tan\left(\frac{\boldsymbol{\theta}_{\boldsymbol{s}}^{\boldsymbol{Ud}}}{2}\right)=\frac{\sin(\boldsymbol{\theta}_{\boldsymbol{s}}^{\boldsymbol{Ud}})}{1+\cos(\boldsymbol{\theta}_{\boldsymbol{s}}^{\boldsymbol{Ud}})}=\frac{\sqrt{1+\mathrm{b}^2}-1}{\mathrm{b}} \tag{26}$$

Therefore, comparing Eqs. (23) and (26), the following expression can be obtained:

$$\boldsymbol{\theta}_{\boldsymbol{s}}^{\boldsymbol{oU}}=-\frac{1}{2}\boldsymbol{\theta}_{\boldsymbol{s}}^{\boldsymbol{Ud}}=-\arctan(\frac{\sqrt{1+\mathrm{b}^2}-1}{\mathrm{b}}) \tag{27}$$

Then the change of the maximum principal strain from the original configuration to the deformed configuration can be obtained accordingly:

$$\boldsymbol{\theta_s^{od}} = \boldsymbol{\theta_s^{oU}} + \boldsymbol{\theta_s^{Ud}} = \arctan\left(\frac{\sqrt{1+\mathrm{b}^2}-1}{\mathrm{b}}\right) \tag{28}$$

From Eqs. (22) to (28), it is proved that $\boldsymbol{\theta_s^{od}} = -\boldsymbol{\theta_s^{oU}} = \boldsymbol{\theta_s^{Ud}}/2$. This means the principal strain axes rotation angle is different with the element rotation angle, and both angles are related to the shear strain. This rotation of principal strain axes will eventually induce the rotation of principal stress axes. The simplification from simple shear to pure shear has failed to address the stress state changes and the relation between the vertical load F and the stress components (σ_{22}, σ_{12}). Therefore, the effective stress calculation is inaccurate when the principal axes keep changing, and the stress components are not available.

The above explanations are all within the central infinitesimal element. When taking the overall deformed area into consideration, however, due to the stress concentration effect, the material does not deform uniformly , as mentioned by several researchers [16, 17, 19, 23], which is also observed during the experimental investigation as shown in Fig. 2b. With the measurement of vertical load *F*, only average stress along the ligament can be obtained, but the average stress cannot accurately reflect the real material behaviour. Therefore, the nonuniformity factor is another error source for the effective stress-strain calculation.

3.2. Strain measurement methods used in the VNR shear test

From the experimental perspective, the measurable variables and related characterisation methods are also essential for assessing the experimental methods and analysing the calculation errors. In the shear tests, the measurable variables include the vertical load F which is a stress-related variable, and the strain or the strain field of the deformed material, depending on the strain measurement methods.

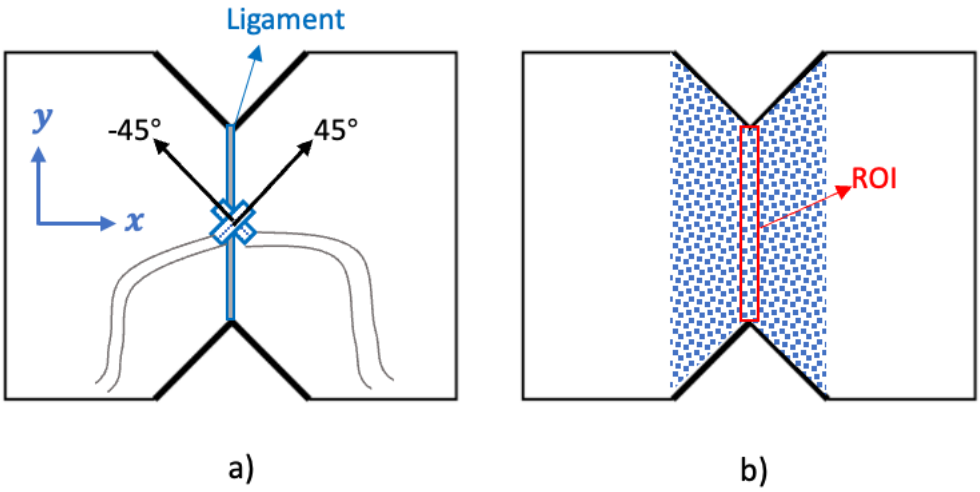

Fig. 6. The shear strain measurement methods in the VNR shear test. a) Using strain gauge; b) Using DIC.

According to the testing standard ASTM 7078 [3] of the VNR shear test, the shear strain can be measured using two strain gauges mounted along the +45° and -45° directions to the loading axis at the ligament centre, shown as Fig. 6a. According to the basic rule of strain transformation, the strains along the +45° and -45° directions can be written as:

$$\varepsilon_{+45^\circ} = \frac{\varepsilon_x+\varepsilon_y}{2} + \frac{\varepsilon_x-\varepsilon_y}{2}\cos(2\times(+45°)) + \frac{\gamma_{xy}}{2}\sin(2\times(+45°)); \quad (29\text{-}1)$$

$$\varepsilon_{-45^\circ} = \frac{\varepsilon_x+\varepsilon_y}{2} + \frac{\varepsilon_x-\varepsilon_y}{2}\cos(2\times(-45°)) + \frac{\gamma_{xy}}{2}\sin(2\times(-45°)), \quad (29\text{-}2)$$

where, ε_{+45° and ε_{-45° are strains measured from the +45° and -45° strain gauges, respectively. The strains of $\varepsilon_x, \varepsilon_y$ and γ_{xy} are the strain components of the analysed element at the specimen centre in the $x-y$ plane shown in Fig. 6a. Subtracting Eq. (29-1) from Eq. (29-1), the maximum shear strain (γ_{xy}) of the analysed element can be obtained as:

$$\gamma_{xy} = \varepsilon_{+45^\circ} - \varepsilon_{-45^\circ} \quad (30)$$

Theoretically, if the centre element is under pure shear deformation mode, +45° and -45° are two principal axes of the deformed element (analysed in Section 3.1). Therefore, two opposite values should be obtained from these two strain gauges. Taheri-Behrooz et al. [19] analysed the strains obtained by two strain gauges in the VNR shear test at a small deformation degree (less than 2%), and the two strain gauges gave the same absolute value but opposite in sign, which showed that within small deformation, it is acceptable to simplify the simple shear to pure shear deformation mode. However, the absolute values of the two strain gauges differ from each other with the increase of deformation due to the rotation of principal axes.

Another commonly used strain measurement method is the DIC method, as shown in Fig. 6b and stated in Section 2.2. For this strain measurement method, the test specimen is pre-processed by creating a speckle grayscale distribution on the target deformation area, and the images of the speckled area are captured during the deformation. After that, an image processing algorithm is applied to the captured images to obtain the strain field. Finally, the shear strain of the specimen is calculated by the average strain over the region of interest (ROI). Under the pure shear assumption, the shear strain equals the maximum principal strain in magnitude. Therefore, the maximum principal strain is normally employed to calculate the effective strain. The size and shape of ROI are defined differently in different studies. For example, while conducting the VNR shear tests, Nunes et al. [12] defined the ROI as a small central zone on the ligament; Filho et al. [24] defined the ROI as five evenly distributed subregions along the ligament; Daiyan et al. [9] defined the ROI as a circle at the centre with a radius of 1-2% of the ligament length (31 mm for standard specimen); Totry et al. [25] defined the ROI as a rectangular at 25 mm × 2 mm in the middle of the ligament.

To summarise, researchers adopted various methods with different technical details to obtain the shear strain of the VNR shear test. These measurement methods are important factors influencing the calculation errors of the VNR shear test as they are using different measured data from various deformation regions on the specimen.

Based on the above mechanism and strain measurement analysis, it was found to be difficult to establish the calculation method for obtaining the real material properties, using only the obtained experimental data, and the error would vary with different strain measurement methods. To have a clear view of the stress-strain field of the VNR shear test specimen and evaluate the calculation error, the numerical simulation on the VNR shear test was conducted due to its ability to show the full field stress/strain data of the deformation.

4. Numerical simulations

4.1. Temperature-dependent Johnson-Cook constitutive model

The effective stress-strain curve proceeded from the tensile tests at 180 ℃ was used to define the material constitutive model for the studied materials. The constitutive model was established as a linear elastic part followed by a nonlinear plastic flow. A temperature-dependent Johnson-Cook (JC) plastic model [26], [27] was employed and calibrated using the tensile test data. The mathematic form of the temperature-dependent JC model between T_g and T_m is given below:

$$\sigma^0 = [A + B(\bar{\varepsilon}^{pl})^n]\left(1 - \left(\frac{\theta-\theta_{ref}}{\theta_{melt}-\theta_{ref}}\right)^m\right), \theta_{ref} < \theta < \theta_{melt}, \quad (31)$$

where the flow stress, σ^0, is a function of the plastic strain, $\bar{\varepsilon}^{pl}$, and the temperature, θ. The terms θ_{ref} and θ_{melt} are material constants representing the reference temperature and the melting temperature, respectively. All temperatures in this model are in absolute temperatures. The terms A, B, n, m are the material constants to be determined.

To identify the material constants, the yield stress and yield strain need to be determined first. Fig. 3 reveals that there is no obvious yield point for PEEK material at the test condition. Therefore, the extrinsic yield point introduced by Brinson et al.[11] was used to identify the yield stress and yield strain of the PEEK specimen under tension. The extrinsic yield point was identified by extrapolating the tangent line of points in the stress-strain curve, and locating the point when the intersection of the tangent line with the x-axis is -0.01. The elastic modulus was defined by the slope of the line connecting the undeformed point (i.e., origin) and the extrinsic yield point. With the yield properties identified, an in-house MATLAB code was developed to identify the JC model constants. The *lsqnonlin* function in MATLAB was adopted to solve the nonlinear least-squares problem. The specific material model parameters are listed in Table 2. The flow stress-plastic strain curves of the experimental result and the fitted model are shown in Fig. 7.

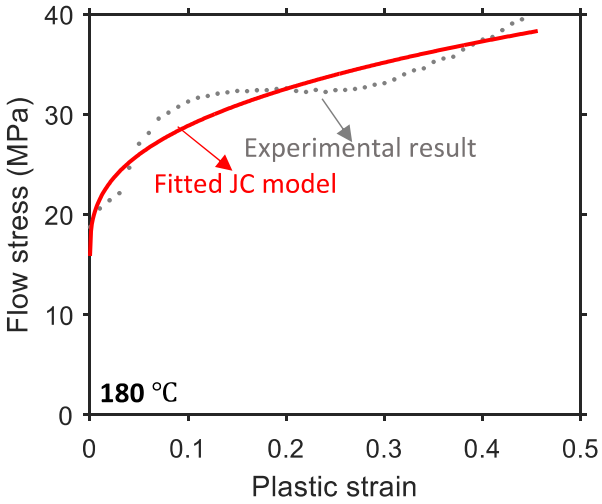

Fig. 7. Flow stress comparison between the JC numerical model and the experimental result of PEEK at a temperature of 180 ℃ and at a strain rate of 0.1 /s.

4.2. Finite element model set-up

In ABAQUS, the virtual specimen was modelled as a deformable part with five integration points through the thickness of the specimens. The 4-node shell element with reduced integration (S4R) was used to define the mesh, and there were 6283 elements in total in the whole model. The numerical

boundary condition was consistent with the experimental setup. Displacement control was applied to the sample during the simulation, and the total displacement was defined as 5 mm. The model was solved using the explicit solver in a Windows system with four CPUs. The total CPU time for completing one case was around 64 minutes. The input parameters required for this model are listed in Table 2.

Table 2. Input parameters required for the VNR shear test simulation

Properties	Parameters
Density (tonne/mm^3)	$\rho = 1.3 \times 10^{-9}$
Modulus (MPa)	$E = 415.948$
Poisson's ratio	$\nu = 0.48$
John-Cook model parameters	*A*=15.651,
	B=29.079,
	n=0.298,
	m =0.947,
	θ_{ref}= 453K (180 ℃)
	θ_{melt} = 616 K (343 ℃)
Predefined field temperature	453 K (180 ℃)

4.3. Model validation

To validate the correctness of the simulation results, the strain distribution and the vertical load were compared with the experimental results for the VNR shear test on PEEK. The maximum principal strain distribution proceeds from numerical simulation, and the experimental results obtained from the DIC analysis were also compared at four deformation stages, as presented in Fig. 8a. These four deformation stages were selected by coordinating the experimental and simulation results, with an interval of around 0.7 mm. The region of 0 to 1 represented the relative position on the ligament of the specimen, with 0 refers to the lower end and 1 refers to the upper end. Fig. 8b and 8c show the strain field measured from the experiment and simulation, respectively, at a certain stage of displacement equals 1.98 mm. The vertical loads obtained from the experiment and simulation are compared in Fig. 8d. The comparison between the experimental and numerical results shows that the strain fields of the numerical results (solid lines) and the experimental results (dot lines) agree with each other well, and vertical loads of both the experimental and numerical results are also consistent, which demonstrates that the numerical simulation results are valid.

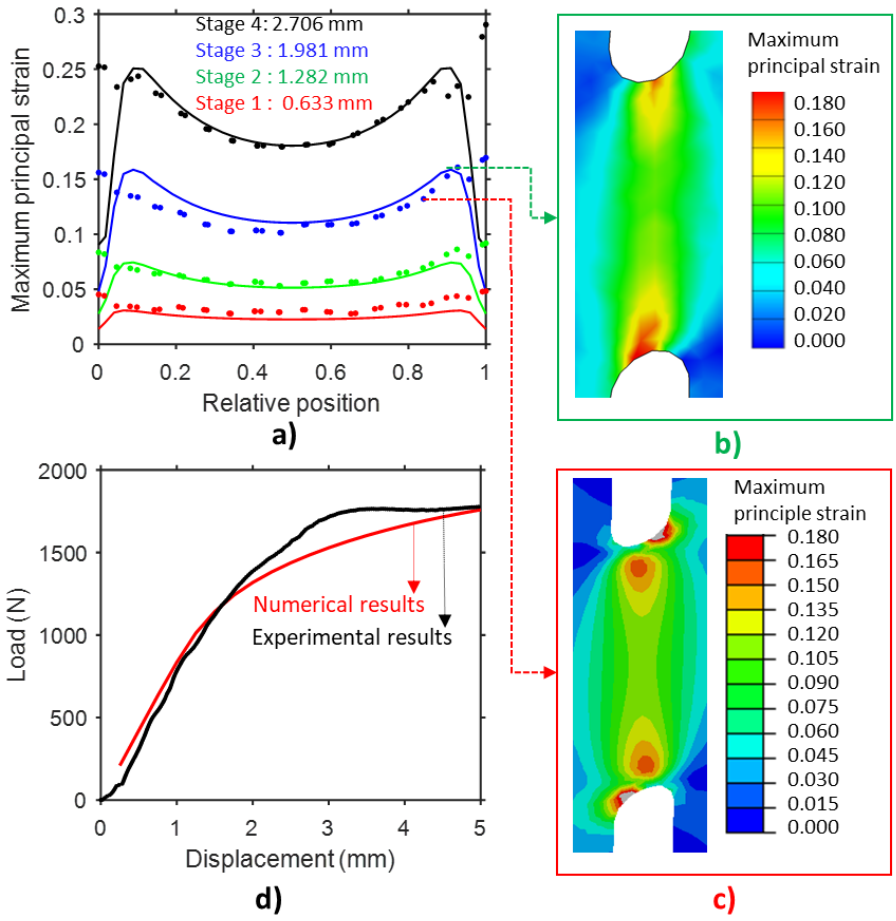

Fig. 8. Validation of the numerical model by comparing a) strain distribution along the ligament at four displacement stages (Solid lines are the numerical results; Dot lines are the experimental results); strain fields of b) experimental and c) numerical results at Stage 3; d) vertical loads obtained from experimental and numerical results.

5. Error analysis and a new correction method

5.1. Analysis of the deformation state of tested materials

The forming limit diagram is normally used to analyse the deformation state of the material. According to the strain field on the specimen shown in Fig. 9a, there is strain localisation along the ligament, making it reasonable to choose two representing nodes for analysis. The two representative nodes on the ligament are the strain localised point near the upper end and the central point of the ligament, i.e., Node 1 and Node 2, respectively. The maximum and minimum principal strains of these two nodes at different deformation stages are presented in Fig. 9b. The green reference line at a slope of -1 represents the strain state under pure shear deformation. It can be observed that Node 2, which is also the central point of the ligament, is under shear state almost during the whole deformation procedure. In contrast, Node 1, which is the strain localised point near the upper end, deflects the shear state at an early stage and starts to deviate from the reference line (green line) when the minimum principal strain equals to c.a. 0.25. Therefore, the central point should be chosen to analyse the real material properties under shear loading.

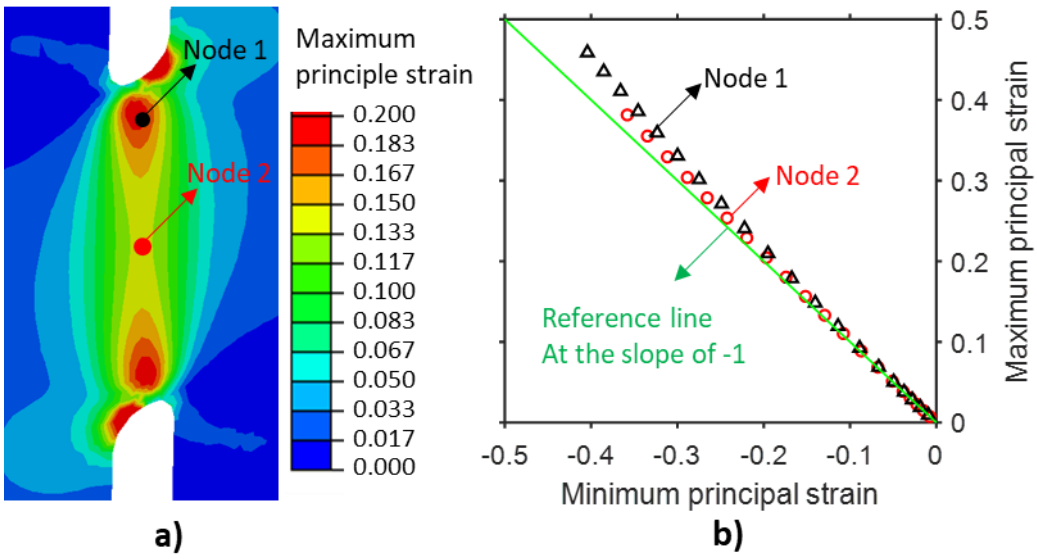

Fig. 9. The deformation state of two representing nodes, Node 1 and Node 2, on the test specimen: a) illustration of the analysed nodes, and b) deformation state of the two analysed nodes in the forming limit diagram.

5.2. The analytical ground truth and error source

From the numerical simulation results, the strain and stress state of each node can be extracted for further analysis. Therefore, to obtain the effective stress-strain curves of the central point, three principal strains and three principal stresses were extracted against each deformation stage. The effective strains (ε_c) and effective stresses (σ_c) of the central point were calculated according to Eqs.(1) and (2) , respectively.

The ground truth of this material property is the input constitutive JC model. The comparison of the central point data and the input model data are shown in Fig. 10. The effective stress-strain curve of the central point agrees well with the input constitutive JC model. Therefore, the properties extracted from the ligament central point can be used as the ground truth property of the studied material. Consequently, corrections need to be made on the effective stress-strain curve calculated from the experimental results to obtain the effective stress-strain curve of the central point.

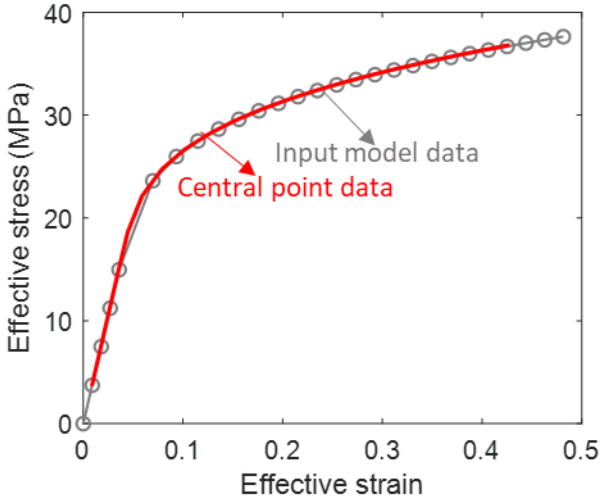

Fig. 10. The ground truth validation: effective stress-strain curves of the central point (Node 2 in Fig. 9) and the input constitutive model (the JC model).

As mentioned in Section 3.2, the characterisation results are also influenced by the measurement methods. Therefore, it is worth identifying the calculation errors for both measurement methods corresponding to the experimental procedures. For experiments using the strain gauge measurement, as explained by Eq.(*30*), the measured strain is actually the maximum shear strain, which equals to the maximum principal strain under the pure shear assumption. Therefore, by adopting the method listed in Eqs. (3) to (14), the effective strain (ε_{SG}) and effective stress (σ_{SG}) are calculated as:

$$\varepsilon_{SG} = \frac{2}{\sqrt{3}} \cdot \gamma_{m-c}\,; \tag{32}$$

$$\sigma_{SG} = \sqrt{3}\frac{F}{A_0}\left(1 + \frac{2}{\sqrt{3}}(e^{\varepsilon_{SG}} - 1)\right); \tag{33}$$

where γ_{m-c} is the maximum shear strain of the central point. The term F is the measured vertical load. The term A_0 is the initial area of the cross-section along the ligament of the specimen. The term $\left(1 + 2(e^{\varepsilon_{SG}} - 1)/\sqrt{3}\right)$ in Eq. (33) is the process of converting the engineering stress to true stress.

For the experiments using DIC measurement, the ROI is defined by the central section, i.e., a node set composed of all the nodes along the central line of the ligament, corresponding to the experimental calculation in Section 2.3. With a similar method explained in Section 2.3, the effective strain (ε_{DIC}) and effective stress (σ_{DIC}) are calculated as:

$$\varepsilon_{DIC} = \frac{2}{\sqrt{3}}\bar{\varepsilon}_{ROI}\,; \tag{34}$$

$$\sigma_{DIC} = \sqrt{3}\frac{F}{A_0}\left(1 + \frac{2}{\sqrt{3}}(e^{\varepsilon_{DIC}} - 1)\right); \tag{35}$$

where $\bar{\varepsilon}_{ROI}$ is the arithmetic mean of maximum principal strains of all nodes in the ROI. The term $\left(1 + 2(e^{\varepsilon_{DIC}} - 1)/\sqrt{3}\right)$ in Eq. (35) is also the process of converting the engineering stress to true stress.

The effective strains and the effective stresses measured by strain gauges and DIC during shear tests are compared with the ground truth data obtained from the central point during tensile tests, as shown in Fig. 11. It demonstrates that no matter which measurement method is used, for the effective strain, the measured strain through the strain gauge and DIC agree well with the ground truth, whereas for the effective stresses, the measured stress through the strain gauge and DIC are quite different from the ground truth. As indicated in Fig. 11b, when the effective strain is higher than 0.102, the calculation errors are nonnegligible, and errors of both measurement methods, i.e., ξ_{SG} and ξ_{DIC},

are observed as around 12.3%. Therefore, a correction method is required for the effective stress calculation at large deformation of the VNR shear test.

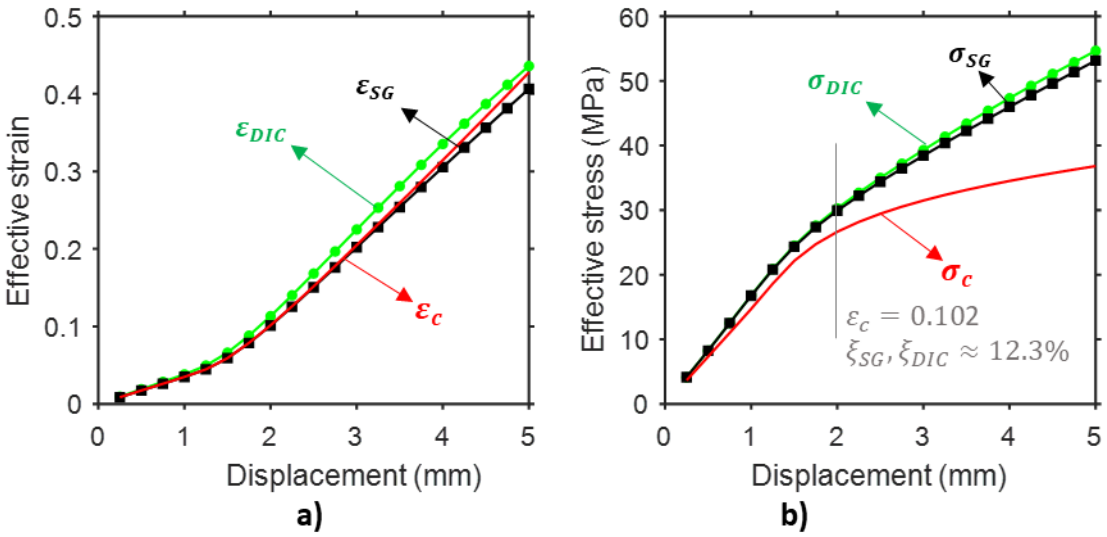

Fig. 11. Comparison between the results of strain gauge and DIC measurements and the ground truth of material properties: a) effective strains and b) effective stresses.

5.3. A new two-step correction method

As explained in Section 3.1, the errors of characterisation results by simple shear tests come from two main factors: the rotation factor and the nonuniformity factor. Also, Fig. 11 has indicated that the main error is introduced through the calculation of effective stress. This section proposes a two-step correction method to correct the two factors that caused the calculation error of effective stress characterised by the VNR shear test. The detailed process is shown in Fig. 12. And the detailed calculation variables are listed in Table 3.

Without considering the nonuniformity, the effective stress should be the average stress of all the nodes on the ligament, as the measured load consists of contributions from all nodes. Therefore, for the rotation factor, the first step of the correction aims to convert the initial calculations, presented in Eqs. (33) and (35), into the effective stress that considering every single node in the ROI. A virtual state is built up as the target curve of this correction step. The effective strain of the target curve (ε_{lg}) is defined by the average value of maximum principal strains ($\bar{\varepsilon}_{m-lg}$) of all nodes in the ROI, while the effective stress of the target curve (σ_{lg}, Eq. (40)) is defined by the averaged value of maximum principal stresses ($\bar{\sigma}_{m-lg}$) of all the nodes in the ROI. With this aim, the first step is to establish the relationship between the errors and the rotational angles of the whole deformation element shown in Fig. 12a)-1 and 12a)-2. The rotational angle is also illustrated as $\Delta\theta_{12}$ in Fig. 5, and can be calculated geometrically from the maximum shear strain as shown in Eq.(6). The calculation of the rotation angle for the target curve, using strain gauges or DIC results is listed as Eqs.(36-38), respectively, where $\bar{\gamma}_{m-lg}$ refers to the mean maximum shear strain values of all the nodes in the ROI. The differences between Eqs.(37) and (38) is caused by the difference between the available data of these two different measurement methods. For the strain gauge measurement, only one set of data is obtained (γ_{m-c}), whereas, for the DIC measurement, the strain data of all nodes inside the ROI are utilised. As for the calculation errors, for both sets of data, the errors should equal to the ratio of the initial effective stresses (σ_{SG}, σ_{DIC}) and the target effective stresses (σ_{lg}). The errors related to the rotational angle are illustrated in Fig. 12a)-2. Here the correction factor regarding the rotation

influence is proposed as the reference line in Fig. 12a)-2 (Eq.(41) or (42)). It is worthwhile to mention that, although Eqs. (41) and (42) are in the same exponential form, the calculated results could be different as these two equations take different input data. The results after the correction on the rotation factor are shown in Fig. 12a)-3. It is obvious that the rotation correction factor works well for both measurement methods.

For the nonuniformity factor, the objective of the correction is to adjust the effective stresses after the first step correction (σ_{SG}^{corr1} and σ_{DIC}^{corr1}) to match the ground truth of the material properties. Therefore, the target curve of this step is the effective stress-strain (σ_c and ε_c) curve of the central point of the specimen, i.e., the ground truth. Although this step aims to deal with the nonuniformity influence, it is still reasonable to do the similar step as the first step correction, since Fig. 8a shows that the strain localisation is also highly related to the shear strain, which simplifies the form of the correction factor. The second step of the correction process is presented in Fig. 12b)-1 and 12b)-2. In this step, the rotational angle for the target curve (ω_c) is calculated using the maximum shear strain of the central point (γ_{m-c}). Similar to the first step correction, the nonuniformity correction factor related to the rotational angles is calculated by obtaining the ratio of the present effective stress (σ_{SG}^{corr1} and σ_{DIC}^{corr1}) and the target effective stress (σ_c). The correction factor corresponding to the nonuniform deformation is shown as the reference line in Fig. 12b)-2, which is calculated via Eq (46) or (47). The results after the correction on the nonuniformity factor are shown in Fig. 12b)-3. It can be clearly observed that, the effective stress-strain curve of the VNR shear test can be corrected to the ground truth of the material properties using the two-step correction based on the experimentally measured data, regardless of the measurement methods. Besides, Fig. 12b)-3 shows that for experiments with strain measured by DIC method (green line), the final results show more reliability at large deformation compared with the strain gauge measurement (black line), which is because more nodes are considered inside the ROI, and the results are more robust.

Table 3. Details of the two-step correction method

Variables	The target curve	Using strain gauges (SG)	Using DIC
The first step correction			
Rotational angle	$\omega_{lg} = \arctan\left(\frac{\tan(\bar{\gamma}_{m-lg})}{2}\right)$ (36)	$\omega_{SG} = \arctan\left(\frac{\tan(\gamma_{m-c})}{2}\right)$ (37)	$\omega_{DIC} = \arctan\left(\frac{\tan(\bar{\gamma}_{m-lg})}{2}\right)$ (38)
Effective strain	$\varepsilon_{lg} = \frac{2}{\sqrt{3}} \cdot \bar{\varepsilon}_{m-lg}$ (39)	ε_{SG} (Eq. (32))	ε_{DIC} (Eq. (34))
Effective stress before correction	$\sigma_{lg} = \sqrt{3} \cdot \bar{\sigma}_{m-lg}$ (40)	σ_{SG} (Eq. (33))	σ_{DIC} (Eq.(35))
The first correct factor	\	$f_{SG}^{1} = e^{\frac{\omega_{SG}}{2}}$ (41)	$f_{DIC}^{1} = e^{\frac{\omega_{DIC}}{2}}$ (42)
Effective stress after the first step correction	\	$\sigma_{SG}^{corr1} = \frac{\sigma_{SG}}{f_{SG}^{1}}$ (43)	$\sigma_{DIC}^{corr1} = \frac{\sigma_{DIC}}{f_{DIC}^{1}}$ (44)
The second step correction			
Rotational angle	$\omega_{c} = \arctan\left(\frac{\tan(\gamma_{m-c})}{2}\right)$ (45)	ω_{SG}	ω_{DIC}
Effective strain	ε_{c} (Eq. (1))	ε_{SG}	ε_{DIC}
Effective stress before correction	σ_{c} (Eq.(2))	σ_{SG}^{corr1}	σ_{DIC}^{corr1}
The second correct factor	\	$f_{SG}^{2} = e^{\frac{2\cdot\omega_{SG}}{3}}$ (46)	$f_{DIC}^{2} = e^{\frac{2\cdot\omega_{DIC}}{3}}$ (47)
Effective stress after the second step correction	\	$\sigma_{SG}^{corr2} = \frac{\sigma_{SG}^{corr1}}{f_{SG}^{2}}$ (48)	$\sigma_{DIC}^{corr2} = \frac{\sigma_{DIC}^{corr1}}{f_{DIC}^{2}}$ (49)

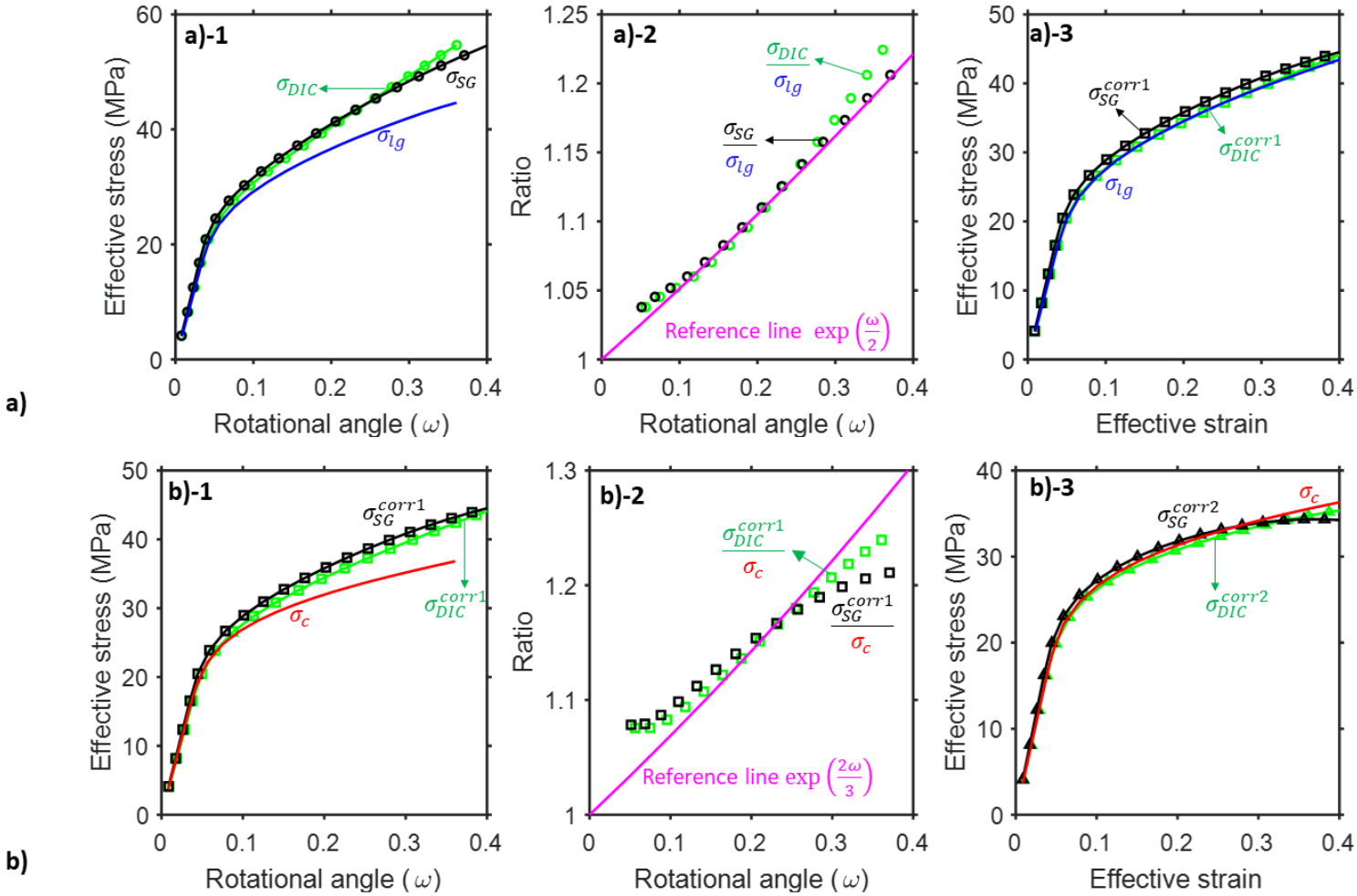

Fig. 12. Two-step correction for the effective stress-strain curves measured using strain gauge and DIC. a) The 1st correction step: a)-1, The relationship between effective stresses and rotational angle; a)-2, The relationship between the calculation errors and rotational angle; a)-3, The first step correction effect; b) The second correction step: b)-1, The relationship between effective stresses and rotational angle; b)-2, The relationship between the calculation errors and rotational angle; b)-3, The second step correction effect.

Fig. 13 shows the comparison of the effective stress-strain curves of strain gauge and DIC methods before and after the two-step correction.

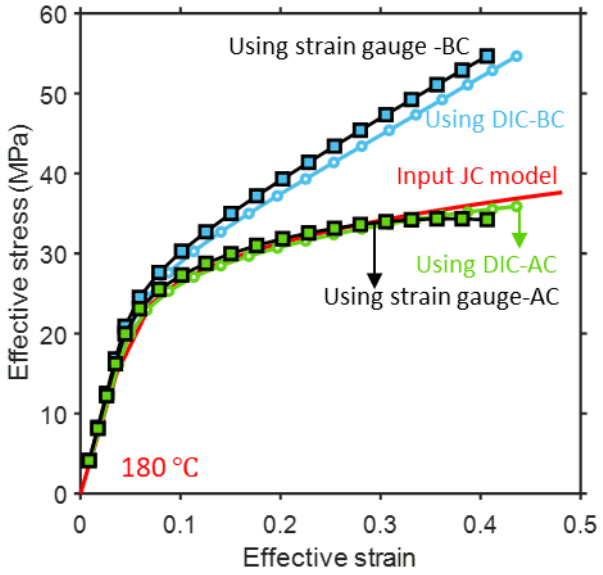

Fig. 13. Comparison of the effective stress-strain curves of strain gauge and DIC methods before and after the two-step correction. (BC means before correction, and AC means after correction).

The above correction process is analysed and calculated according to numerical results. As the initial problem indicated in Fig. 3, the effective stress-strain curves calculated from the tensile and the VNR shear test data are considerably different without the correction procedure. Therefore, by adopting the two-step correction method proposed above, the shear test results can be corrected. The effective stress-strain curves under tensile and the VNR shear tests on PEEK at 180 ℃ is shown in Fig. 14. Compared to Fig. 3, the characterised material properties after corrections show more reliability.

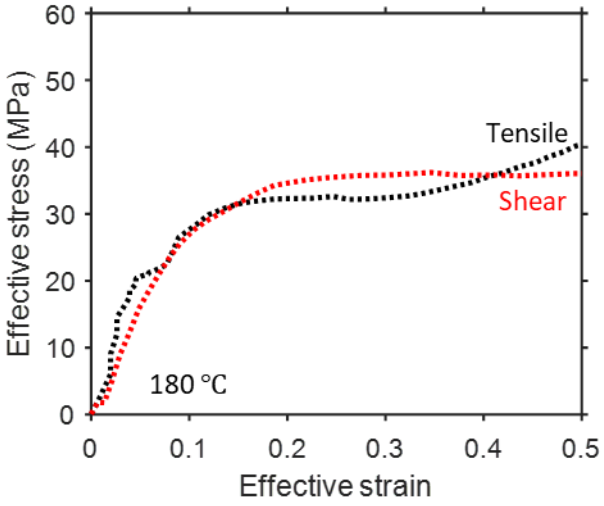

Fig. 14. The effective stress-strain curves of the tensile and the VNR shear tests (after the two-step correction) on PEEK at a temperature of 180 ℃ and at a strain rate of 0.1/s. (The uncorrected results are shown in Fig. 3.)

5.4. Validation of the developed correction method

To further validate the correction method, the model constants fitted from the corrected and uncorrected VNR shear test data were entered into ABAQUS, to show the detailed difference of the final material properties before and after correction. Fig. 15 shows the JC model fitting results using the experimental data before and after correction. The fitted material parameters are listed in Table 4. The most notable difference is shown by the n parameter in JC model, representing the strain hardening exponent, which is also bolded in Table 4. Without the correction, the strain hardening exponent, n, might be more than twice of the real value. The numerical simulation setup is the same as the previous setup described in Section 4.2.

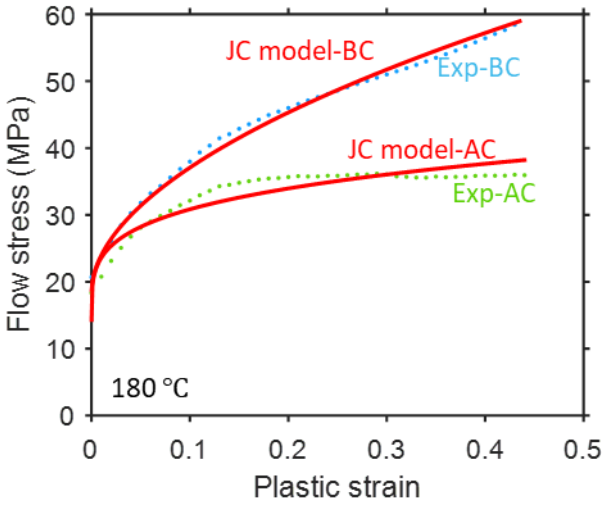

Fig. 15. Flow stress-plastic strain curves obtained from the JC model predicted results and the VNR shear experimental results at a temperature of 180 ℃ and a strain rate of 0.1/s. (BC means before correction, AC means after correction. Exp refers to the experimental results)

Table 4. Input parameters required for the numerical simulations (using the VNR shear test data)

Properties	Parameters before correction	Parameters after correction
Density (tonne/mm3)	$\rho = 1.3 \times 10^{-9}$	$\rho = 1.3 \times 10^{-9}$
Modulus (MPa)	$E = 372.314$	$E = 312.559$
Poisson's ratio	$\nu = 0.48$	$\nu = 0.48$
Johnson-Cook model parameters	*A*=18.517,	*A=14.032*,
(*A, B, n, m,* θ_{ref}, θ_{melt})	*B=62.864*,	*B=29.569*,
	n=0.530,	***n*=0.245,**
	m =0.652,	*m* =0.675,
	θ_{ref}= 453K (180 ℃)	θ_{ref}= 453K (180 ℃)
	θ_{melt} = 616 K (343 ℃)	θ_{melt} = 616 K (343 ℃)
Predefined field temperature	453 K (180 ℃)	453 K (180 ℃)

The simulation results regarding these two sets of model input parameters were analysed and compared with the experimental results obtained from the DIC measurement. Similar to the previous analysis, the maximum principal strain distribution along the ligament was analysed at four displacement stages shown in Fig. 16a and 16b, respectively. Under small deformation, i.e., when the displacement is lower than that defined in the first deformation stage (the effective strain is around 0.093 at this stage), the strain distributions are similar

regardless of the model is fitted for uncorrected or corrected test data. However, with the deformation increases, the model output begins to deflect the experimental results with the model fitted using the uncorrected testing data. Besides, the results show that the extent of deflection increases with the increasing deformation. In contrast, with the model fitted from the corrected testing data, the predicted strain fields comply with the experimental results very well.

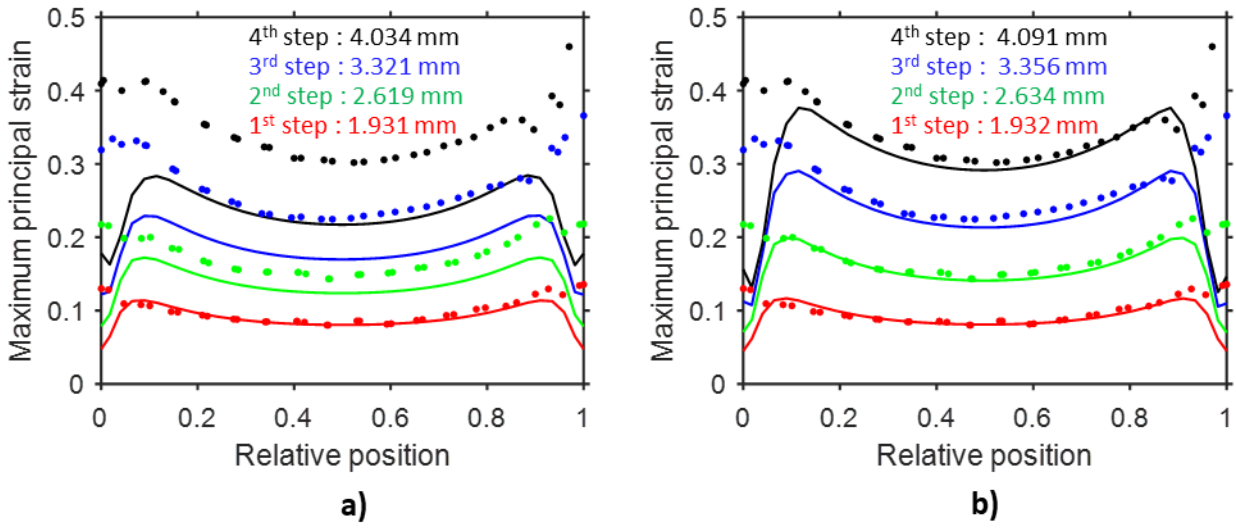

Fig. 16. Comparison between experimental and numerical results using shear test results as model input at 180 ℃: strain field comparison at four displacement stages using a) model fitted using uncorrected shear test data and b) model fitted using corrected shear test data. (The solid lines are the numerical results, and the dot lines are the experimental results.)

The above analysis and validation are all based on the material properties of PEEK at 180 ℃. To further validate the universality of the two-step correction method on the post-processing of the VNR shear test results against other conditions and even on different materials, another two groups of simulation were conducted: 1) the PEEK material at 240 ℃; 2) the PA6 material at 160 ℃. As mentioned in Section 3.1, tensile tests on PEEK at 240 ℃ and PA6 at 160 ℃ were also conducted. The JC model parameters of PEEK are the same as listed in Table 2. The JC model constants of PA6 were also calibrated by the tensile test results. The parameters required for these two sets of simulation are listed in Table 5.

Table 5. Input parameters required for the numerical simulations
(using tensile test results of the validation materials)

Properties	Parameters of PEEK at 240 ℃	Parameters of PA6 at 160 ℃
Density (tonne/mm^3)	$\rho = 1.3 \times 10^{-9}$	$\rho = 1.5 \times 10^{-9}$
Modulus (MPa)	$E = 167.295$	$E = 180.13$
Poisson's ratio	$\nu = 0.48$	$\nu = 0.48$
John-Cook model parameters	*A*=15.651,	*A*=11.489,
(*A, B, n, m,* θ_{ref}, θ_{melt})	*B*=29.079,	*B=14.531*,
	n=0.298,	*n=0.729*,
	m =0.947,	*m* =1.079,
	θ_{ref}= 453K (180 ℃)	θ_{ref}= 433K (160 ℃)
	θ_{melt} = 616 K (343 ℃)	θ_{melt} = 503 K (230 ℃)

Predefined field temperature	513 K (240 ℃)	433 K (160 ℃)

Fig. 17 compares the effective stress-strain curves of these two validation simulations before and after correction. There are similarities between Fig. 13 and Fig. *17*, in which the effective stress-strain curves without correction always deflect from the ground truth at large deformation, regardless of the strain measurement methods. By adopting the two-step correction method on post-processing of the VNR shear test data, the correct material properties can be obtained against different conditions or even with different materials.

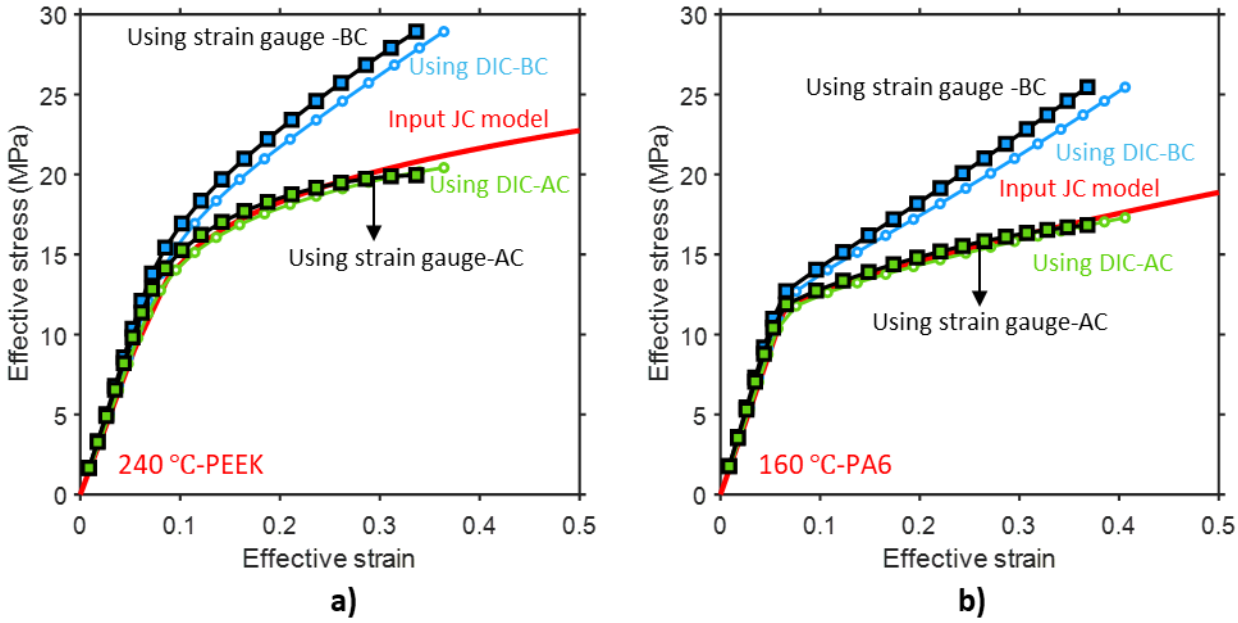

Fig. 17. Verification of the correction method by a) changing the test condition of the same material (PEEK); and b) changing the material (PA6). (BC means before correction, and AC means after correction).

6. Conclusions

In this study, the mechanism of the simple shear deformation was analysed. The rotation factor and the non-uniformity factor were identified as error sources. The tensile experiments, the V-Notched Rail (VNR) shear experiments and simulations were performed to quantify these two factors. A two-step correction method is proposed for post-processing of the VNR shear test results to obtain the real effective stress-strain properties. The main conclusions are drawn as follows:

1) There is rigid-body rotation during the simple shear deformation, and the rotation angle of the deformation is related to the shear deformation. Therefore, the rotation factor is an important factor that influences the characterisation of the material properties. Besides, the nonuniformity of deformation is another nonnegligible factor that can affect the characterisation results.

2) Through the numerical simulation using ABAQUS, the full stress/strain field can be extracted, and therefore the post-processing errors can be quantified. It is found that, when the simple shear was simplified as pure shear, there are significant errors in the effective stress calculation of the VNR shear test, especially at large deformation (when the effective strain is higher than 0.1).

3) A two-step correction method is proposed to mitigate the two error sources, i.e., the rotation factor and the nonuniformity factor. The correction factors for the two influential factors are all in an exponential relationship to the rotation angle, which can be calculated from the shear strain.

4) The numerical validation on the two-step correction method has been conducted using material models fitted from the VNR shear test results, before and after correction. The correlation between the experimentally and numerically obtained strain fields confirmed the validity of this two-step correction method. Besides, this two-step correction method is also validated by the same material at a different condition and different thermoplastic materials, which demonstrates the robustness of the proposed correction method.

Acknowledgement

Hongyan Wang acknowledges the financial support from the Chinese Scholarship Council (CSC) and Imperial College London. Zerong Ding acknowledges the funding support from Shougang-Imperial Lab for lightweight steel-based systems for impact resistant automotive applications at Imperial College London.

References

1. Moreira D.C., Nunes L.C.S., *Comparison of simple and pure shear for an incompressible isotropic hyperelastic material under large deformation.* Polymer Testing, 2013. **32**(2): p. 240-248.
2. Thiel C., et al., *Shear, pure and simple.* International Journal of Non-Linear Mechanics, 2019. **112**: p. 57-72.
3. *ASTM D7078/D7078M-12 Standard Test Method for Shear Properties of Composite Materials by V-Notched Rail Shear Method*. 2012, ASTM International: West Conshohocken, PA.
4. *ASTM D4255 / D4255M-01(2007), Standard Test Method for In-Plane Shear Properties of Polymer Matrix Composite Materials by the Rail Shear Method*. 2007, ASTM International: West Conshohocken, PA.
5. De Baere I., W., Van Paepegem, Degrieck J., *Design of a modified three-rail shear test for shear fatigue of composites.* Polymer Testing, 2008. **27**(3): p. 346-359.
6. *ASTM D5379 / D5379M-19e1, Standard Test Method for Shear Properties of Composite Materials by the V-Notched Beam Method*. 2019: West Conshohocken, PA.
7. Maurel-Pantel A., et al., *A thermo-mechanical large deformation constitutive model for polymers based on material network description: Application to a semi-crystalline polyamide 66.* International Journal of Plasticity, 2015. **67**: p. 102-126.
8. Jones D.F., Treloar L.R.G., *The properties of rubber in pure homogeneous strain.* Journal of Physics D: Applied Physics, 1975. **8**(11): p. 1285-1304.

9. Daiyan H., et al., *Shear Testing of Polypropylene Materials Analysed by Digital Image Correlation and Numerical Simulations.* Experimental Mechanics, 2012. **52**(9): p. 1355-1369.
10. Nunes L.C.S., *Mechanical characterization of hyperelastic polydimethylsiloxane by simple shear test.* Materials Science and Engineering: A, 2011. **528**(3): p. 1799-1804.
11. Brinson H.F., Brinson L.C., *Polymer engineering science and viscoelasticity : an introduction*. 2018, New York: Springer.
12. Nunes L.C.S., *Modified slotted shear test for a thin sheet of solid polymer under large deformations.* Polymer Testing, 2015. **45**: p. 20-30.
13. Belytschko T., Liu W.K., and B. Moran, *Nonlinear Finite Elements for Continua and Structures*. 2000: John Wiley & Sons, Ltd.
14. Rajagopal K.R., Wineman A.S., *New universal relations for nonlinear isotropic elastic materials.* Journal of Elasticity, 1987. **17**(1): p. 75-83.
15. G'Sell C., Dahoun A., *Evolution of microstructure in semi-crystalline polymers under large plastic deformation.* Materials Science and Engineering: A, 1994. **175**(1): p. 183-199.
16. Hedner G., Seldén R., Lagercrantz P., *Shear test for thermoplastic polymers.* 1994. **34**(6): p. 513-518.
17. Melin N., *The modified Iosipescu shear test for orthotropic materials*. 2008, KTH.
18. Oh J.H., et al., *Interlaminar Shear Behavior of Thick Carbon/Epoxy Composite Materials.* Journal of Composite Materials, 1999. **33**(22): p. 2080-2115.
19. Taheri-Behrooz F., Moghaddam H.S., *Nonlinear numerical analysis of the V-notched rail shear test specimen.* Polymer Testing, 2018. **65**: p. 44-53.
20. *ASTM D638-14 Standard Test Method for Tensile Properties of Plastics*. 2014, ASTM International: West Conshohocken, PA.
21. Wang H., et al., *Experimental and constitutive modelling studies of semicrystalline thermoplastics under solid-state stamp forming conditions.* Polymer, 2021. **228**: p. 123939.
22. Barba D., Arias A., Garcia-Gonzalez D., *Temperature and strain rate dependences on hardening and softening behaviours in semi-crystalline polymers: Application to PEEK.* International Journal of Solids and Structures, 2020. **182-183**: p. 205-217.
23. Ho H., et al., *Numerical analysis of the Iosipescu specimen for composite materials.* Composites Science and Technology, 1993. **46**(2): p. 115-128.
24. Filho J.C.A.D., Nunes L.C.S., *Simple shear response of a thin sheet of polytetrafluoroethylene under large deformations.* Polymer Testing, 2019. **78**: p. 105942.
25. Totry E., et al., *Effect of fiber, matrix and interface properties on the in-plane shear deformation of carbon-fiber reinforced composites.* Composites Science and Technology, 2010. **70**(6): p. 970-980.
26. Chen F., et al., *Hot tensile fracture characteristics and constitutive modelling of polyether-ether-ketone (PEEK).* Polymer Testing, 2017. **63**: p. 168-179.
27. Garcia-Gonzalez D., et al., *Mechanical impact behavior of polyether–ether–ketone (PEEK).* Composite Structures, 2015. **124**: p. 88-99.